Design and Characterization of Metal-Nanoparticle Infiltrated Mesoporous Metal-Organic Frameworks

Juby R. Varghese,[a] Christian Wendt,[b] Fletcher B. Dix,[a] Darpandeep Aulakh,[a] Uta Sazama,[c] Andrey A. Yakovenko,[d] Michael Fröba,[c] Jörn Wochnowski,[b] Dan V. Goia[a] and Mario Wriedt[a,*]

[a] Department of Chemistry & Biomolecular Science, Clarkson University, Potsdam, New York 13699, United States. E-mail: mwriedt@clarkson.edu

[b] Technische Hochschule Lübeck, Fachbereich Angewandte Naturwissenschaften, 23562 Lübeck, Germany

[c] Institute of Inorganic and Applied Chemistry, University of Hamburg, Martin-Luther-King-Platz 6, 20146 Hamburg, Germany

[d] X-ray Science Division, Advanced Photon Source, Argonne National Laboratory, Argonne, IL 60439, United States

*Corresponding author, e-mail: mwriedt@clarkson.edu

Abstract

The infiltration of palladium and platinum nanoparticles (NPs) into the mesoporous metal-organic framework (MOF) CYCU-3 through Chemical Vapor Infiltration (CVI) and Incipient Wetness Infiltration (IWI) processes was systematically explored as a means to design novel NP@MOF composite materials for potential hydrogen storage applications. We employed a traditional CVI process and a new "green" IWI process using methanol for precursor infiltration and reduction under mild conditions. Transmission electron microscopy-based direct imaging techniques combined with synchrotron-based powder diffraction (SPD), energy-dispersive X-ray spectroscopy (EDS), and physisorption analysis reveal that the resulting

NP@MOF composites combine key NP and MOF properties. Room temperature hydrogen adsorption capacities of 0.95 and 0.20 mmol/g at 1 bar, and 2.9 and 1.8 mmol/g at 100 bar are found for CVI and IWI samples, respectively. Hydrogen spillover and/or physisorption are proposed as the dominating adsorption mechanisms depending on the NP infiltration method. Mechanistic insights were obtained through crystallographic means using SPD-based difference envelope density (DED) analysis providing previously underexplored details on NP@MOF preparations. Consequently, important host-guest correlations influencing the global hydrogen adsorption properties are discussed and demonstrate that employing MOFs as platforms for NPs is an alternative approach to the development of versatile materials for improving current hydrogen storage technologies.

Introduction

The burning of fossil fuels and its contribution to greenhouse gas emissions have long been a problem scientists seek to remedy. Cleaner alternatives such as hydrogen have been proposed in order to reduce the dependency on fossil fuels due to its natural abundancy and lack of CO_2 emissions.[1, 2] Hydrogen's high gravimetric heats of combustion and renewability make it very attractive in onboard hydrogen storage systems for automotive fuel cell applications.[3] However, hydrogen storage still faces many challenges since its gaseous state and nonpolar nature limits low-energy storage at ambient conditions and thus preventing hydrogen from being a significant competitor against gasoline.

Most established storage technologies currently include compressed hydrogen, liquid hydrogen and absorption-based methods using metal hydride technology.[4] The U.S. Department of Energy (DOE) milestones for 2020 onboard hydrogen storage is 4.5 wt% at a working pressure differential of 12 bar and ambient temperature.[5] Although solid state materials have proven to be promising candidates to meet this target, many challenges still need to be overcome. Metal hydrides absorb hydrogen through chemisorption which results in high hydrogen storage capacities. However, metal hydrides create very strong bonds with hydrogen which can result in significant thermodynamic and kinetic problems upon charging and discharging cycles.[3] Physisorption on the other hand allows for the molecular storage of hydrogen within a porous

support exhibiting large surface areas. Activated carbons,[6, 7] zeolites,[8, 9] porous polymers,[10, 11] various carbon nanostructures,[12, 13] and metal-organic frameworks (MOFs)[14-17] have been investigated as candidates for high-density hydrogen storage.

MOFs are crystalline porous materials composed of metal clusters or ions bridged by organic linkers into multidimensional frameworks.[18] Their key features include large pore volumes and surface areas which can be fine-tuned by the choice of metal and organic building blocks.[19-21] The permanent porosity allows for adsorption of hydrogen molecules through weak van der Waals interactions resulting in cyclability of the capture and release process for continuous use of the materials. In 2003, Yaghi *et al*. reported the first MOF for hydrogen storage[22] and hundreds of MOFs have been investigated for this application in the intervening years.[1, 23, 24] These materials open up exciting avenues for structural diversity and tunability and expand the understanding and application of porous supports for hydrogen storage applications.

Since DOE targets focus on ambient storage temperatures, this provides an additional challenge as most MOFs only show significant hydrogen uptake at 77 K. At cryogenic temperatures, there is a strong interaction between hydrogen and the MOF surface allowing for reports of hydrogen uptake exceeding the DOE target amount. The primary force is physisorption where van der Waals forces and other intermolecular forces are dominant. Generally, this type of adsorption is weak and reversible and the hydrogen uptake capacity strongly correlates with the specific surface area of the MOF.[1] For example, MOF-177 exhibits a surface area of 4500 m^2/g and adsorbs 19.6 wt% H_2 at 77 K and 100 bar. At room temperature, however, the uptake capacity is reduced to 0.6 wt%.[25] This general phenomenon can be attributed to thermal motion effects resulting in significantly lower hydrogen uptake capacities which impedes storage capabilities where physisorption is the dominating force at ambient conditions.[1, 3]

To address this challenge, composite materials such as metal nanoparticle (NP) infiltrated MOF systems are of interest. These materials are referred to as NP@MOF composites. For example, Pt[26, 27] and Pd[28, 29] NPs are well known for their superior hydrogen absorption properties due to the dissociation and spillover effect of hydrogen molecules into monatomic hydrogen.[3, 30] Coupling of this unique behavior with

the high surface areas of the MOFs is the driving force in the design of NP@MOF composites.[31, 32] However, as these are high-boiling metals and MOFs show only limited temperature stability, selecting a suitable functionalization process such as CVI or IWI is a crucial component to avoid structural damage of the MOF.

MOFs are an advantageous support to host NPs because they provide precise control of NP aggregation *via* their tunable structures, pore environments and functionalities and these advantages are lacking in previously explored porous materials such as zeolites and mesoporous silicas.[33] As a key feature, the well-defined cavities of MOFs can limit agglomeration and stabilize these NPs in a confined environment facilitating the formation of monodispersed NPs within the MOF. The cavities are usually large enough to not only host NPs but also to facilitate mobility of hydrogen in the pore space allowing hydrogen sorption on surfaces of both the MOF and the metal NP itself.[34] The most established method for designing NP@MOF composites is the post-synthetic infiltration of metal precursors into the cavities of MOFs followed by the reduction of the precursors into elemental metal. The size of NPs is controlled by the MOF pores without structurally altering them through the subsequent functionalization process. However, one of the significant challenges with this technique is NP deposition on the surfaces of MOF particles rather than infiltration into pores. This was commonly found to occur in microporous MOFs (<2 nm pores).[34] Therefore, expanding this approach to mesoporous MOFs (>2 nm pores) provides an increased opportunity for the preferred precursor adsorption into their pore system.

Herein we systematically designed and characterized new NP@MOF composites based on platinum and palladium NPs, and the thermally and chemically robust mesoporous MOF $[Al(OH)(SDC)]_n$ (H_2SDC = 4,4′-stilbenedicarboxylic acid) or CYCU-3 as the host.[35] CYCU-3 consists of two different 1D channel pores, hexagonal mesopores of 3.1 nm diameter spaced by triangular micropores of 1.4 nm diameter (**Figure 1a**). Previously, we also explored this MOF as a host for the controlled nanostructuring of single molecule magnets.[36-38] Two distinct processes for the infiltration of NPs into CYCU-3 were investigated: Chemical Vapor Infiltration (CVI)[39, 40] and Incipient Wetness Infiltration (IWI).[41, 42] NP precursors platinum(II) acetylacetonate and palladium(II) hexafluoroacetylacetonate (**Figure 1b, c**) were used for the

CVI process. For the scope of this investigation, humid environments were not considered and samples were prepared with minimal exposure to air. In the first step of CVI, precursors were sublimed into the gas phase, followed by their adsorption into the MOF pores by a vacuum process, and final formation of Pd/Pt-NPs initiated by a controlled thermal decomposition process. The advantage of CVI *vs*. physical processes like PVD (Physical Vapor Deposition) is that NPs can be infiltrated under very mild thermal conditions and therefore, allowing CVI to be readily used for the subsequent functionalization of MOFs. Different experimental setups for precursor infiltration were employed to explore effects on the hydrogen uptake. For the IWI process, a previously unexplored procedure was utilized: methanol mediated infiltration of the precursor hexachloroplatinic(IV) acid into the pores of the framework at ambient conditions (**Figure 1d**) followed by its reduction into Pt-NPs under very mild heating conditions, with methanol also functioning as the reducing agent allowing the transition from Pt^{4+} to Pt^{0}. As the use of methanol was previously unexplored as both a carrier solvent used in precursor loading and as an aid in the reduction of Pt-NPs, the IWI process was crystallographically probed for mechanistic insights governing the precursor infiltration and reduction process. Selected samples were further characterized for high pressure (100 bar) hydrogen adsorption at 233 and 298 K. Although numerous NP@MOF composites have been investigated in order to enhance or alter the properties of the individual components, to date only a few crystallographic studies report on the structural characterization of precursor infiltrated MOFs,[43, 44] whereas no studies have looked at the holistic process from precursor infiltration to NP formation. Furthermore, we want to highlight the novelty and simplicity of our NP formation process for IWI featuring methanol as a two-in-one solution simultaneously acting as a precursor carrier solvent and a reducing agent.

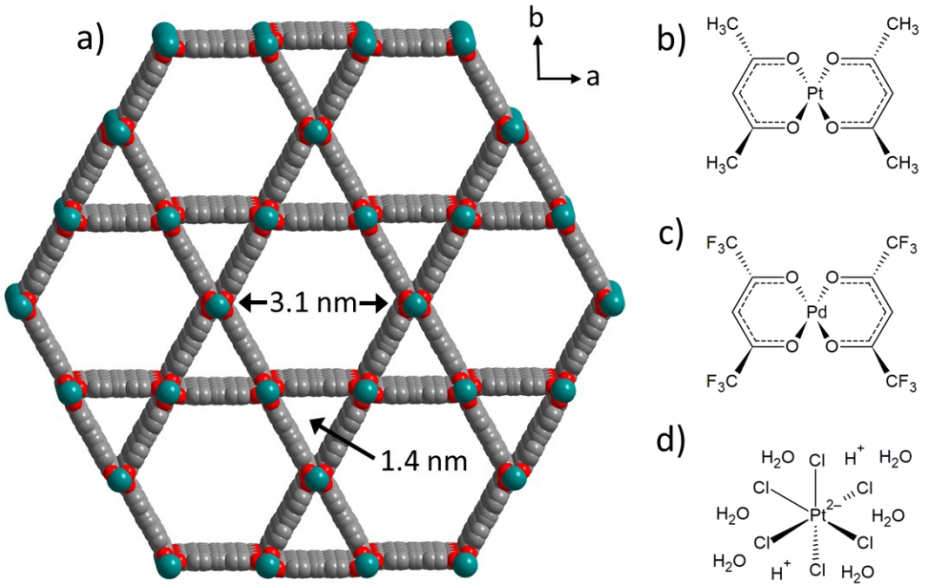

Figure 1. Structures of single-components used for NP@MOF synthesis. (a) Crystal structure of mesoporous MOF CYCU-3 in space fill mode with view along the hexagonal and trigonal channel pores, and (b-d) Lewis structures of NP-precursors platinum(II) acetylacetonate, palladium(II) hexafluoroacetylacetonate and hexachloroplatinic(IV) acid, respectively.

Experimental Section

General

All reagents and solvents were used without further purification. CYCU-3 was synthesized as previously reported.[35] The purity of the bulk material was confirmed by PXRD (**Figure S1**).

Synthesis

Chemical Vapor Infiltration (CVI). The infiltration of Pt and Pd precursors (platinum(II) acetylacetonate and palladium(II) hexafluoroacetylacetonate) into CYCU-3 was performed by loosely packing 50 or 100 mg of as-synthesized CYCU-3 in the center of a glass tube (25 cm length, 0.9 cm diameter) and placing glass wool on both sides of the MOF to constrain its central position. For sample activation, the tube was sealed on one side and wrapped with heating tape followed by heating at 150 °C for 2 h under vacuum at

10^{-7} bar using a Pfeiffer HiCube 80 Eco Turbo Pumping Station (**Figure S2a**). After heating, the tube was cooled to RT and flushed with N_2 (UHP grade) for 15 min. This activation process was employed for double-sided, mixed, and rotational infiltration. Masses of precursors and MOF used and details of applied temperature-time programs for precursor infiltration and reduction are listed in **Table S1**. All individual batches of composites were well mixed after synthesis to obtain optimal phase homogeneity and stored in glass vials under N_2.

The experimental setup for *double-sided infiltration* is shown in **Figure S2b**. An appropriate amount of Pd precursor was added to side 1 of the activated MOF tube and constrained with glass wool. For precursor@MOF formation, the tube was heated at 50 °C for the allotted time under vacuum at 10^{-7} bar. After heating, the tube was cooled to RT and flushed with N_2 for 15 min. Following this process, the tube was flipped and sealed on side 1 and opened on side 2 where a second batch of Pd precursor was added. The same temperature-time program was repeated. For NP@MOF formation, the tube was heated at 200 °C for the allotted time followed by cooling to RT, leaving under vacuum at room temperature for 1 h to remove the organic precursor components and flushing with N_2 for 1 h before the sample was removed from the tube affording Pd-NP@MOF composites.

The experimental setup for *mixed infiltration* is shown in **Figure S2c**. The glass wool was carefully removed from one side of the activated MOF tube and an appropriate amount of Pd or Pt-precursor was added and mixed with the activated MOF which was then re-sealed with glass wool. For precursor@MOF formation, the tube was heated at 50 °C (for Pd) and 130 ºC (for Pt), respectively, for the allotted time under vacuum at 10^{-7} bar. Following this process for NP@MOF formation, the tube was heated at 200 °C (for Pd) and 300 ºC (for Pt), respectively, for the allotted time followed by cooling to RT, leaving under vacuum at room temperature for 1 h to remove the organic precursor components and flushing with N_2 for 1 h before the sample was removed from the tube affording Pd- and Pt-NP@MOF composites, respectively.

The experimental setup for *rotational infiltration* is shown in **Figure S2d.** An appropriate amount of Pd precursor was added to one side of the activated MOF tube and constrained with glass wool. For precursor@MOF formation, this tube was placed in a temperature controlled rotating chamber and heated

at 50 °C for the allotted time under vacuum at 10^{-6} bar using a Vacuubrand rotary vane oil pump. Following this process for NP@MOF formation, the tube was heated at 200 °C for the allotted time followed by cooling to RT, leaving under vacuum at room temperature for 1 h to remove the organic precursor components and flushing with N_2 for 1 h before the sample was removed from the tube affording Pd-NP@MOF composites.

Incipient Wetness Infiltration (IWI). Methanolic stock solutions of Pt-precursor hexachloroplatinic(IV) acid was prepared in concentrations of 200, 500, and 1000 ppm. 20 mL portions of these solutions were slowly added to batches of 100 mg of CYCU-3 under rapid stirring and was kept stirring at RT for 24 h. The resulting yellow powders were separated by filtration, washed with methanol until the filtrate was colorless to remove any excess precursor and dried under vacuum yielding precursor@MOF. These powders were each placed in 20 mL of methanol and refluxed at 70 °C for 24 h. The resulting grey powders were separated by filtration, washed with methanol until the filtrate was colorless to remove any excess NPs and dried under vacuum yielding Pt-NP@MOF composites. All samples were stored in glass vials under N_2.

Characterization

Powder X-ray Diffraction (PXRD). PXRD data was collected on a Bruker D2 Phaser diffractometer equipped with a Cu sealed tube (λ = 1.54178 Å). Powder samples were dispersed on low-background discs for analyses.

Gravimetric Methanol Adsorption. Methanol adsorption measurements were performed using a modified TG analyzer setup with a TGA Q50 from TA Instruments. All measurements were performed using platinum crucibles in a dynamic nitrogen atmosphere (50 mL/min) and a heated or cooled at a rate of 3 °C/min. The instrument was corrected for buoyancy and current effects and was calibrated using standard reference materials. For activation, an as-synthesized sample of CYCU-3 was heated to 280 °C and cooled to RT

followed by subjection to methanol vapors until the mass stabilized. The sample was re-heated to 280 °C to investigate its desorption process.

Low-Pressure Gas Adsorption. Gas adsorption isotherms for pressures ranging from $1 \cdot 10^{-5}$ to 1 bar were measured volumetrically using a Micromeritics ASAP2020 surface area and pore analyzer. Pre-weighed analysis tubes were charged with samples, each capped with a seal frit, and heated at 150 °C under a dynamic vacuum for 24 h. For all isotherms, warm and cold free-space correction measurements were performed using He gas (UHP grade). N_2 and H_2 (both UHP grade) isotherms at 77 K were measured using a liquid nitrogen bath, and H_2 isotherms at 295 K were measured using a water bath. The specific surface areas were determined from BET fits using the 0.05-0.15 relative pressure range of N_2 adsorption isotherms at 77 K, while incremental pore size distributions were determined from DFT methods for slit pores.

High-Pressure Gas Adsorption. The volumetric high pressure H_2 adsorption measurements were carried out on a BELSORP High Pressure Gas Adsorption Measuring System in combination with a Julabo deep-freeze circulating thermostat FP89-ME in a pressure range up to 110 bar. The samples were activated at 200 °C in oil pump vacuum for 24 h before analysis and they remained in the instrument and were not thermally treated between subsequent adsorption cycles.

Transmission Electron Microscopy (TEM). TEM images were measured with a JEOL JEM 2010F at an accelerating voltage of 200 kV. Sliced samples were prepared using a Leica ultramicrotome to slice 80 nm thin slices with a Diatome diamond knife and loaded on a Lacey-carbon-coated Cu grid. ImageJ software was used to process TEM images in order to determine the metal nanoparticle sizes.

Elemental Mapping. Elemental mapping analyses were performed with a Thermo NORAN System Six EDS coupled to a JEOL JSM-7400F field-emission scanning electron microscope (FESEM) set to an acceleration voltage of 15 kV and a working distance of 8 mm.

Energy-Dispersive X-ray spectra (EDS). SEM-EDS were recorded using an Oxford EDS Detector 65 mm^2 coupled to a JEOL JSM-7900FLV SEM with a low vacuum backscatter electron detector (LVBED) set to an accelerating voltage of 15 kV and a working distance of 8 mm. 5 data points were selected for SEM-EDS measurements and analyzed for elemental composition in terms of weight percentage using AZtecLive Ultim Max 65 mm^2 software.

Synchrotron Powder Diffraction (SPD) with Difference Envelope Density (DED) Analysis. CYCU-3 samples can only be obtained as polycrystalline material, single crystal structure analysis cannot be employed. Hence, high-quality powder diffraction patterns of as-synthesized CYCU-3, precursor@MOF and NP@MOF composites were recorded on 17BM beamline at the Advanced Photon Source, Argonne National Laboratory (Argonne, IL, USA). The incident X-ray wavelength was 0.72768 Å. Data were collected using a Perkin-Elmer flat panel area detector (XRD 1621 CN3-EHS) over the angular range 1-11° 2-theta. The data reveals that the crystallinity and crystal structure of CYCU-3 remains intact upon NP infiltration. The unit cell parameters of CYCU-3 and NP@MOF samples differ only very slightly (**Table S2**). Rietveld analyses of NP@MOF composites could not be applied to determine adsorption sites of NPs due to their low occupancy. Instead the Difference Envelope Density ρ_Δ method was applied.[36, 37, 45, 46] Le Bail refinements were performed in Jana2006[47] using the initial unit-cell parameters a = 34.298, c = 6.312 Å and space group $P6_3/mmc$ as taken from our previous study.[36] The unit cell parameters, zero-point shift, background, and peak profile (pseudo-Voigt) were refined. Upon the reach of satisfactory profile fits and R-factors (**Table S2, Figures S3-S5**), reflections integrated intensities (F^2_{obs}) were extracted and used for generation of Structure Envelope (SE) densities (see SI for details).

Results and Discussion

Platinum and palladium NPs were selected for the controlled and systematic infiltration into the mesoporous MOF CYCU-3. Resulting NP@MOF composites were investigated for their expected enhanced hydrogen

adsorption capabilities at ambient conditions as compared to the pristine MOF. The dominating effects attributed to the enhancement of hydrogen adsorption capacities is still controversial with hydrogen spillover being the most frequently discussed mechanism for materials containing Pd[48-50] and Pt,[39, 51, 52] whereas the formation of metal hydrides is also discussed as a potential mechanism.[50, 53, 54] However, hydrogen spillover within MOFs is still not well understood.[34, 52, 55] The design of NP@MOF composites allows for the advantageous combination of hydrogen uptake from both metal NPs and MOFs. The high specific surface areas of MOFs allow for hydrogen gas to be physisorbed onto the pore walls, while the NPs allow for molecular hydrogen to dissociate and spillover into monoatomic hydrogen followed by the migration of the hydrogen atoms onto the framework.[56] These two factors combined have the potential to enhance hydrogen storage capacities of MOFs but also other applications such as NP-based catalysis.

Pd/Pt-NP@MOF Synthesis *via* Chemical Vapor Infiltration (CVI). CVI is a two-step process involving the adsorption of selected organometallic precursors into the MOF by low-temperature sublimation followed by a controlled thermal decomposition of the precursors to form elemental metal NPs.[57] Pd-NPs are well-known for their significant hydrogen storage capabilities which led us to select palladium(II) hexafluoroacetylacetonate as precursor for CVI. Preliminary infiltration and reduction experiments showed that the samples were not homogenously infiltrated with some sections of the MOF remaining white, indicating minimal to no loading. Our observation is not commonly discussed in literature, in fact, many investigations relied on general color change and did not disclose whether a gradient was present within the sample before additional handling, such as mixing the sample, which is a vital first indicator in uniform precursor loading.[57, 58] Therefore, we explored different experimental setups to probe uniform loading and how the nature of infiltration impacts the hydrogen uptake capacities of resulting NP@MOF composites.

The as-synthesized MOF was loosely packed in a stationary glass tube and constrained with glass wool. The MOF was activated prior to any infiltration experiment. This process involves heating the MOF at 150 °C for 2 h under dynamic vacuum. The completion of this process was confirmed by tracking the mass loss upon activation. In following systematic infiltration experiments three techniques were employed:

(1) double-sided, (2) mixed, and (3) rotational infiltration. Details on these setups can be found in the experimental section. In the double-sided setup, infiltration was performed by flowing the sublimed precursor through the activated MOF from both tube directions. In the mixed setup, the precursor and activated MOF were mixed together prior to sublimation and infiltration of the precursor. Since in both of these setups the MOF is stationary, the pore accessibility for the diffusion-controlled infiltration might be limited. To circumvent this, we employed a temperature controlled rotational component which was added to the system in order to rotate the tube during the infiltration process. After precursor infiltration, all techniques include a vacuum-assisted thermal reduction process for NP formation.

All resulting Pd-NP@MOF composites (**Pd-CVI-1** to **Pd-CVI-18**) were screened for their BET surface area and hydrogen adsorption at ambient conditions to obtain insights into how the nature of infiltration technique influences the global hydrogen uptake. Respective BET surface area values and hydrogen uptake capacities are listed in **Table S1** with hydrogen isotherms at 295 K shown in **Figures S6a-c**. As a general trend, we observed a significant reduction in BET surface area from ~3000 m^2/g of pristine CYCU-3 to as low as ~1500 m^2/g which is in agreement with partial pore blocking induced by infiltrated metal NPs. Double-sided and mixed infiltration resulted in composites with hydrogen adsorption capacities at 295 K and 1 bar as high as 0.55 mmol/g (**Pd-CVI-2**) and 0.69 mmol/g (**Pd-CVI-13**), whereas rotational infiltration resulted in only 0.31 mmol/g (**Pd-CVI-17**). These values reflect a significant enhancement of hydrogen adsorption as compared to pristine CYCU-3 showing only 0.15 mmol/g at 293 K and 1 bar (**Figure S7**). This enhancement can be attributed to dominating hydrogen spillover effects as evident from the limited desorption behavior of the Pd-CVI samples.

The Pd precursor-based CVI experiments resulted in Pd-NP@MOF composites with respectable hydrogen uptake capacities with the mixed infiltration process being the most promising CVI technique. Since Pt-NPs are also well-known for their significant hydrogen storage capabilities,[27, 30, 59, 60] we selected platinum(II) acetylacetonate as the alternative precursor for CVI with a specific focus on the mixed infiltration process. The precursor infiltration time was systematically explored followed by thermal reduction to form Pt-NP@MOF composites (**Pt-CVI-1** to **Pt-CVI-3**). A maximum hydrogen uptake capacity of 0.95

mmol/g at 295 K and 1 bar was found after 12 h of infiltration for sample **Pt-CVI-2** with no further increase observed after prolonged infiltration. An overview of the respective BET surface area values and hydrogen uptake capacities of Pt-NP@MOF composites are listed in **Table S1** with hydrogen isotherms at 295 K shown in **Figure S6d**. Similar as found for all **Pd-CVI** samples, it can be concluded that chemisorption is the dominating adsorption process for all **Pt-CVI** as evident from their limited desorption capabilities. Sample **Pt-CVI-2** was selected for further characterization due its highest hydrogen uptake value. Its low-pressure hydrogen isotherm suggests no saturation of adsorption thus making the high-pressure regime of interest for exploration. Three consecutive high-pressure (<100 bar) adsorption-desorption isotherms of **Pt-CVI-2** were collected at 298 K. Respective excess isotherms for adsorption of hydrogen[24, 61] showing type 1 behavior and hysteretic adsorption and desorption are displayed in **Figure S8**. A storage capacity of 2.9 mmol/g (0.59 wt%) is found at 100 bar and 298 K. This represents a significant enhancement as compared to pristine CYCU-3 showing only an uptake of 2.4 mmol/g (0.48 wt%) as displayed in **Figure S11b**. We propose that hydrogen spillover is the dominating adsorption mechanism at high-pressure for **Pt-CVI-2** which is evidenced by the observed hysteretic sorption and limited desorption capability. In addition, it is observed that the sorption properties decline after the first cycle and then stabilize for the second and third cycle. The decline of the 1st cycle in **Pt-CVI-2** may be due slight structural changes such as partial collapse or shrinkage of the MOF structure during high pressure measurements until a stable state is reached. The samples were kept in the apparatus and did not undergo thermal treatment between cycles, therefore thermal activation-based structural collapse can be excluded. It is also possible that the 1st cycle removed potential residual impurities which may have remained after the activation procedure and led to a state with a reproducible accessibility of the active sites and pore surfaces. This is supported by the behavior of the 1st cycle where the adsorption and desorption branches do not form a closed loop, however, this is the case for the 2nd and 3rd cycles.

The next step of this systematic study was comprised of probing the correlation of the NP precursor infiltration time *vs.* different experimental parameters including the (i) NP metal loading capacity, (ii) nitrogen uptake at 77 K, (iii) hydrogen uptake at 295 K, and (iv) available pore volume. Three samples were

selected for each infiltration method and metal: double-sided, **Pd-CVI-2** to **4**; mixed, **Pd-CVI-10** to **12**; and rotational infiltration, **Pd-CVI-16** to **18** and **Pt-CVI-1** to **3**. An additional merit for the above sample selection is that all samples for each of the different infiltrated methods were prepared using comparable conditions: 60 and 70 mg of NP precursor for respective **Pd-CVI** and **Pt-CVI** samples, respectively; and 1, 2, and 4 h of NP precursor infiltration time for respective **Pd-CVI** samples, and 2, 12, and 24 h for respective **Pt-CVI** samples. An overview of all sample preparation details is listed in **Table S1** for reference. The metal loading capacities of the **CVI** samples were probed using SEM-EDS with the respective results plotted in **Figure S13** and the pore volumes were obtained from DFT pore size calculations using nitrogen isotherm data with the respective results plotted in **Figure S12**. In addition, all resulting numerical data are listed in **Table S1** with the respective experimental trends as function of the NP precursor loading time displayed in **Figure S14**.

The NP loading capacities for the **Pd-CVI** samples range from 0.15 to 8.97 wt% while the **Pt-CVI** samples range from 9.52 to 12.86 wt% which indicates that the nanoparticle infiltration is not uniform across the different infiltration methods. In terms of gas uptake in relation to the metal content, no apparent trend is found for all collective **CVI** samples. However, the following trends are found for specific individual infiltration methods: for Pd-based mixed-infiltrated samples (**Figure S14b**), as the Pd content increases, the nitrogen uptake increases and the hydrogen uptake decreases; for Pd-based rotational-infiltrated samples (**Figure S14c**), as the Pd content increases, the nitrogen uptake decreases and the hydrogen uptake increases; and for Pt-based mixed-infiltrated samples (**Figure S14d**), as the Pt content increases, both the nitrogen uptake and hydrogen uptake increases. No trend is observed for the Pd-based double-sided-infiltrated samples (**Figure S14a**). Overall, Pd-based mixed-infiltrated samples show higher Pd content combined with lower hydrogen uptakes, while Pd-based rotational-infiltered samples show lower Pd content combined with higher hydrogen uptakes. This observation is an unexpected relationship as the opposite behavior of higher Pd content, higher hydrogen uptake is expected. We speculate that the used NP loading technique influences how the NPs assemble into the MOF pores. As CYCU-3 has 1D channel pores, it is possible that NPs are predominantly formed at the pore openings as the Pd content increases which can

potentially block hydrogen from entering the pore system and accessing the innermost NPs. This speculation is supported by the accessible pore volume which increases with increasing Pd content for Pd-based mixed-infiltration samples. In addition, a higher metal content can be expected for the mixed-infiltration samples and with it, a higher chance of pore blockage given that this infiltration method originally mixes the NP precursor with the MOF prior to the composite formation.

In summary, this data shows that Pt-NP@MOF composites have a higher intrinsic affinity to hydrogen as compared to Pd-NP@MOF composites, although no general trend could be observed for the explored samples. We believe these results are a valuable addition to the current knowledge of NP@MOFs for hydrogen storage as the majority of reports focus on Pd-based composites.[34]

Pt-NP@MOF Synthesis *via* Incipient Wetness Infiltration (IWI). Pt-NP@MOF composites from CVI experiments above have been identified so far as the most promising hydrogen storage materials within the scope of this investigation. Following this finding, IWI has been explored as an alternative approach to prepare Pt-NP@MOF composites. IWI is regarded as a "green" approach for precursor infiltration since this method requires no application of ultra-high vacuums.[62] In particular, we focused on a method developed by Goia *et al.*[63] which allows the rational design of monodispersed Pt-NPs. Goia described that refluxing methanolic solutions of hexachloroplatinic(IV) acid form quantitatively Pt-NPs with methanol functioning as the reducing agent at a mild temperature of only 70 ºC. To the best of our knowledge this process has not yet been applied for MOFs. Current processes for the reduction of MOF infiltrated Pt-precursors involve harsh conditions such as hydrogen gas treatment at high pressures and temperatures.[34] If Goia's process can be employed for IWI, the advantages are twofold: (1) methanol at ambient conditions can act as carrier solvent for Pt-precursor infiltration into the MOF pores, and (2) upon completion of Pt-precursor infiltration, increasing the temperature of methanol to reflux conditions can reduce the Pt-precursor into monodisperse Pt-NPs. In summary, this method constitutes a very mild and "green" approach for the design of new Pt-NP@MOF composites by IWI.

CYCU-3 was probed by gravimetric methanol adsorption studies to explore its compatibility with Goia's methanol-based process which was confirmed by a remarkable reversible methanol uptake of 55 wt% as shown in **Figure 2**. In addition, CYCU-3 was reported to be stable in methanol.[35] Consequently, we started systematic infiltration and reduction studies with methanol Pt-precursor concentrations of 200, 500 and 1000 ppm resulting in samples **Pt-IWI-1**, **Pt-IWI-2** and **Pt-IWI-3**, respectively. Details on the experimental conditions can be found in the experimental section. The first indication of successful infiltration and reduction could be made visually since the sample processing was accompanied by distinct color changes as shown in **Figure 3**. Upon precursor infiltration, the white-colored methanolic dispersion of CYCU-3 changed into a pale-yellow color, while upon reduction, a dark-grey dispersion was obtained. The same colors could be confirmed for washed and dried samples of respective Pt-precursor@MOF and Pt-NP@MOF composites. Subsequently, the structural integrity of CYCU-3 was probed by PXRD measurements. As displayed in **Figure 4**, no loss of crystallinity can be observed after each respective treatment with the high-angle scans showing broad Bragg reflections characteristic of Pt-NPs as shown in **Figure S9**. In addition, SEM-EDS measurements were performed to probe the Pt loading content in all **Pt-IWI** samples. As a result, the highest Pt content is found for **Pt-IWI-3** (1.95 wt%) followed by **Pt-IWI-1** (0.14 wt%) and **Pt-IWI-2** (0.05 wt%). The respective SEM-EDS spectra are displayed in **Figure S16**.

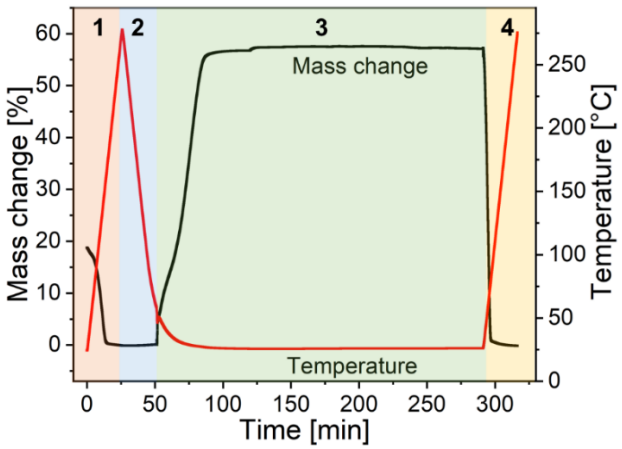

Figure 2. Thermogravimetric methanol adsorption in MOF CYCU-3. The MOF was thermally activated in a dynamic N_2 atmosphere to remove DMF molecules from the pores (area 1), followed by a cooling step to

RT (area 2) and adsorption step by switching the atmosphere to methanol (area 3), and the reversibility of methanol adsorption was probed by a final heating step (area 4).

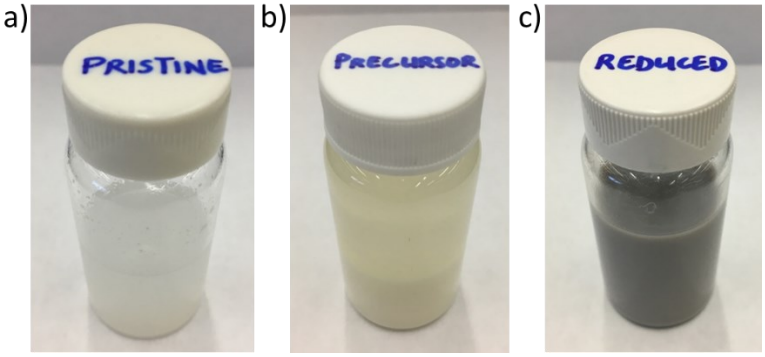

Figure 3. Color change upon two-step Pt-NP@MOF synthesis by IWI. The pristine methanolic MOF-dispersion is white-colored (a), which changes into light-yellow upon Pt-precursor infiltration (b), and finally into dark-grey upon reduction (c).

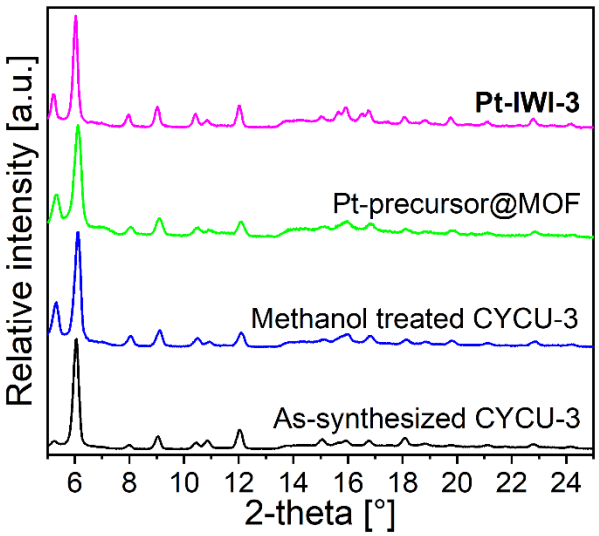

Figure 4. PXRD patterns of MOF CYCU-3 after different treatments (λ = 1.54178 Å). As-synthesized CYCU-3 (black), methanol treated CYCU-3 (blue), Pt-precursor infiltrated CYCU-3 (green), and Pt-NP@MOF sample **Pt-IWI-3** (magenta).

Hydrogen Uptake Studies. All Pt-IWI samples were screened for their hydrogen uptake capacities at ambient conditions. **Pt-IWI-1** and **Pt-IWI-3** showed reasonable enhancements of 0.27 and 0.20 mmol/g (0.05 and 0.04 wt%), respectively, which corresponds to improvements of 80% and 33%, respectively, and no improvement for **Pt-IWI-2** as compared to pristine CYCU-3. This adsorption behavior correlates very well with the respective Pt loading content found from SEM-EDS measurements (**Figure S16d**): **Pt-IWI-1** and **Pt-IWI-3** show the highest Pt contents, while the Pt content in **Pt-IWI-2** is two orders of magnitude less. This observation might be attributed to specific concentrations required for adequate Pt-precursor infiltration into the MOF pores. Certain concentrations most likely do not represent optimal critical mass to allow for saturation of the pores during the infiltration process which can be in turn detrimental to the reduction and hydrogen uptake process. The optimal critical mass is the localized concentration necessary for the diffusion of the precursors to take place within the pores. Although the precursor stock solution concentration is known, the localized concentrations of the precursors near the pores which allow for infiltration are unknown and are further limited if the stock concentration is low. Therefore, if a critical mass is not reached, this will influence the nucleation sites which will then limit NP formation. Respective ambient temperature hydrogen isotherms of all Pt-IWI samples are shown in **Figure 5a**. Noticeably, all samples display a slight hysteretic adsorption and desorption which is archetypal for spillover.[64] In addition, full desorption is observed which is an unusual observation for spillover and might be indicative of a significant physisorption component on the surface of Pt-NPs. For comparison, only very few MOF studies report low-pressure ambient hydrogen storage capacities as MOF-hydrogen affinities are commonly very weak at RT and 1 bar. For example, MOF $Co_2(bdc)_2(dabco)$ adsorbs 0.03 wt% which is a representative value for non-metal infiltrated MOFs.[65]

The hydrogen adsorption properties of Pt-IWI samples were further probed by low-pressure (<1 bar) hydrogen adsorption measurements at 77 K and high-pressure (<100 bar) hydrogen adsorption measurements at 233 and 298 K. Pristine CYCU-3 shows a respectable uptake capacity of 10.6 mmol/g (2.1 wt%) at 77 K and 1 bar as shown in **Figure S7**, whereas samples **Pt-IWI-1**, **Pt-IWI-2** and **Pt-IWI-3** exhibit only values of 4.3, 4.2, and 5.9 mmol/g (0.85, 0.83, and 1.16 wt%), respectively. This trend also correlates

well with the respective Pt loading contents obtained from SEM-EDS measurements (**Figure S16d**), where the higher the Pt content, the higher the hydrogen uptake. Respective hydrogen isotherms at 77 K are shown in **Figure 5b**. The explanation of this observation is based on the drastically reduced surface area in **Pt-IWI** samples due to Pt-NPs partially blocking the pores of CYCU-3, making less surface area available for adsorption as compared to pristine CYCU-3. **Figures S10** and **6a** display respective nitrogen isotherms at 77 K. Thus, it is evident that the dominating adsorption process at low-temperature is of a physisorptive nature and not spillover.

Sample **Pt-IWI-3** was selected for further investigations. Its low-pressure hydrogen isotherm at ambient temperature shown in **Figure 5a** suggests no saturation of adsorption and thus making the high-pressure regime of interest for exploration. High-pressure (<100 bar) isotherms of **Pt-IWI-3** were collected at 233 K and 298 K. Respective excess adsorption isotherms for hydrogen[24, 61] showing type 1 behavior and slight hysteretic adsorption and desorption are displayed in **Figure 5c**. Storage capacities of 2.4 and 1.8 mmol/g (0.48 and 0.36 wt%) are found at 100 bar and, 233 and 298 K, respectively. Interestingly, **Pt-IWI-3** still does not reach saturation of adsorption even at 100 bar, but with almost full desorption observed. Also, considering that pristine **Pt-IWI-3** *vs*. pristine CYCU-3 shows enhanced H_2 adsorption at <1 bar and opposite behavior at 100 bar as shown in **Figures S7** and **S11** respectively, we can conclude that physisorption is the dominating adsorption process at higher pressures but hydrogen spillover remains the dominating adsorption process in the low-pressure regime. This conclusion corresponds well with high-pressure cyclic adsorption and desorption studies performed at 233 and 298 K over each three cycles as shown in **Figure 5d**. Full cyclability is observed which is a unique observation but in agreement with results from ambient low-pressure studies showing full desorption capability. For comparison, it is typical that hydrogen spillover results in irreversible chemisorption such as reported for Pt-NP@MOF-177 with 2.5 wt% at RT and 144 bar in the first cycle followed by only 0.5 wt% in the second cycle.[39] The decrease between cycles was attributed to the formation of Pt hydrides which therefore can be excluded as a potential mechanism for the fully reversible adsorption in **Pt-IWI-3**.

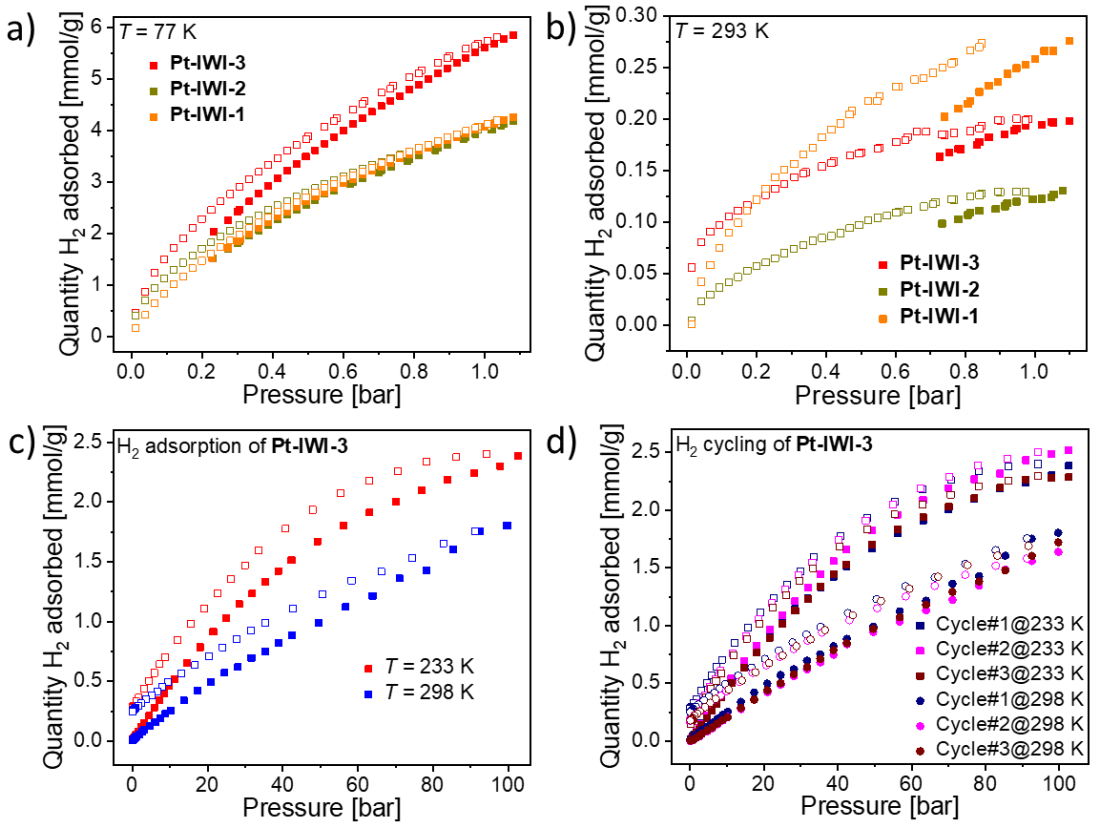

Figure 5. Hydrogen isotherms of Pt-IWI samples. Low-pressure regime at 77 K (a) and 293 K (b), high pressure regime at 233 K and 298 K (c) with adsorption-desorption cycling at same temperatures (d). Solid and open symbols represent adsorption and desorption values, respectively.

Mechanistic Insight into Pt-NP@MOF Formation. The interesting hydrogen storage properties of **Pt-IWI-3** led us to further probe its detailed structure-property relationships. Verifying that Pt-NPs are formed within the MOF pores rather than deposited on the MOF particles' surfaces, and understanding the diffusion and reduction process of Pt-precursors within the MOF matrix is of foremost interest. Three independent experiments were performed, all of which verify that Pt-NPs are effectively formed within the pores of CYCU-3: (1) BET surface area and pore size distribution by nitrogen physisorption analysis, (2) direct-imaging by transmission electron microscopy (TEM), and (3) synchrotron-based powder diffraction (SPD) data combined with investigations on the difference envelope density (DED).

Nitrogen adsorption measurements were employed to investigate the materials surface properties. Respective isotherms at 77 K of pristine CYCU-3, Pt-precursor@CYCU-3 and **Pt-IWI-3** are shown in **Figure 6a**. The isotherms reveal a reversible type IV behavior with one well-defined step at intermediate partial pressures which is characteristic for the coexistence of micro- and mesopores. The BET surface area decreases from 3004 m^2/g in pristine CYCU-3 to 1124 m^2/g in Pt-precursor@CYCU-3 followed by a further decrease to 985 m^2/g upon reduction into **Pt-IWI-3**. This observation is the first evidence that the precursor adsorption and reduction takes place inside the MOF pores. The pore size distribution derived from DFT calculations is consistent with the presence of micro- and mesopores as shown in **Figure 6b**. It is evident that the precursor infiltrates the micro- and mesopores and this can be quantified by a significant reduction in the total pore volume from 1.89 cm^3/g in pristine CYCU-3 *vs.* 0.62 and 0.54 cm^3/g in Pt-precursor@CYCU-3 and **Pt-IWI-3,** respectively.

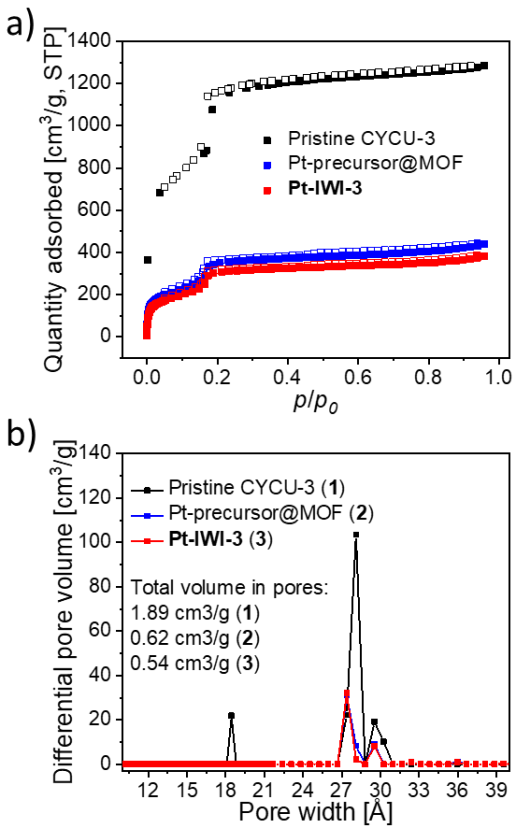

Figure 6. Nitrogen isotherms at 77 K (a) and DFT pore size distributions of pristine CYCU-3, Pt-precursor@CYCU-3 and **Pt-IWI-3** (b).

The location of the Pt-NPs within CYCU-3 was further elucidated by TEM. TEM images of **Pt-IWI-3** were collected due to the contrast of Pt *vs.* the low electron density elements of CYCU-3. The Pt-NPs were found to be dispersed in select domains throughout the material, with some areas that had no visible NPs present. No long-range order observed as displayed in **Figure 7a**. However, even though TEM imaging can confirm the presence of Pt-NPs, it can hardly be distinguished if they are embedded within the MOF pores or being deposited on the MOF particles' surfaces. In order to confirm the former case, ultramicrotomy was employed to obtain ultra-thin sections of the composite. A representative cross-sectional TEM image of an ultra-thin section of **Pt-IWI-3** is shown in **Figure 7b**. Pt-NP images indicate approximate size of 3 nm in the transverse direction which are in the range of the mesopore size of CYCU-3, confirming that the Pt-NPs are embedded within the MOF matrix. This observation also confirms that the pores of CYCU-3 provide a template to control growth and agglomeration of the particles as most imaged Pt-NPs are roughly the mesopore size of 3 nm with the possibility that the framework undergoes partial deformation allowing for slightly larger particles than the apparent pore size. These results corroborate the spillover-dominated low-pressure ambient hydrogen storage properties of **Pt-IWI-3** as it has been reported that smaller sized Pt-NPs are more efficient in their spillover effect.[66] Moreover, as shown in **Figure S15**, SEM elemental mapping has been employed to verify that although sparse, a homogenous distribution of Pt-NPs can be found throughout the composite.

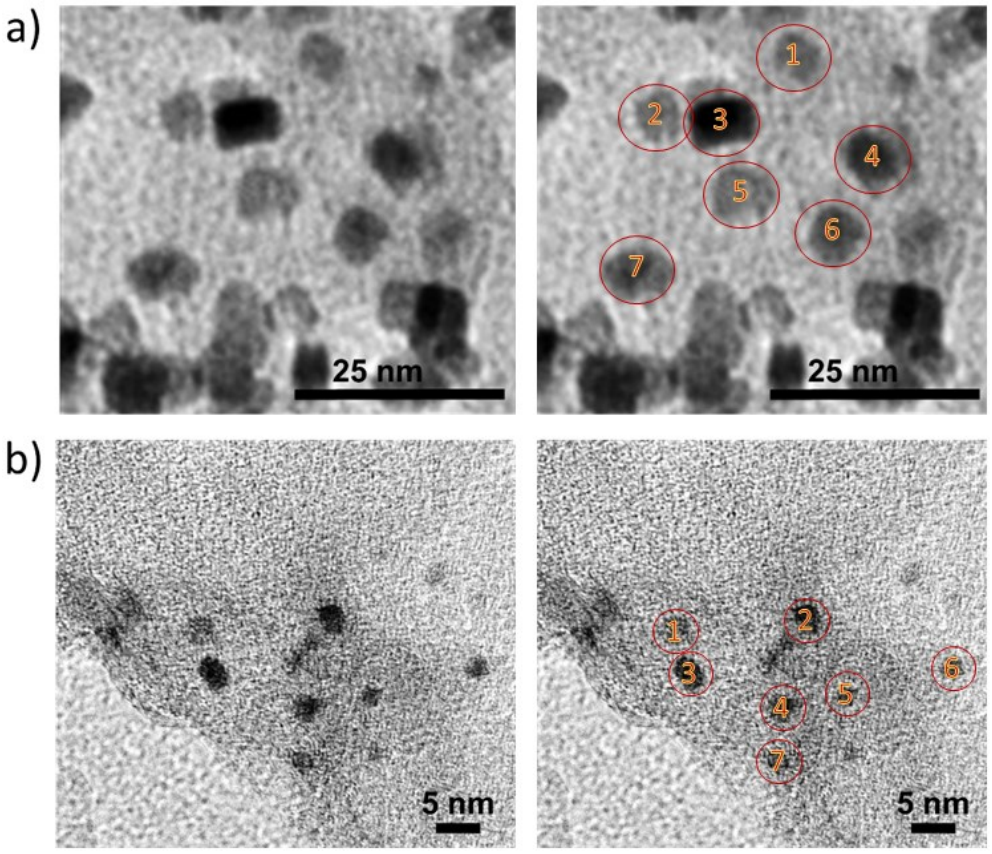

Position	Diameter (nm)
1	2.283
2	2.101
3	3.449
4	2.368
5	3.09
6	2.735
7	3.876
Average: 2.843	

Position	Diameter (nm)
1	3.469
2	2.961
3	3.163
4	2.959
5	2.425
6	2.671
7	2.367
Average: 2.859	

Figure 7. Representative TEM images of an as-synthesized (a) and ultra-thin sliced section (b) of **Pt-IWI-3** with average Pt nanoparticle sizes calculated for each image.

Little is known about the structural characteristics of precursor diffusion and reduction in MOFs. While the analysis of DFT pore size distribution of **Pt-IWI-3** has already confirmed that the Pt-precursor infiltrates into both the micro- and mesopores, we further probed this process by synchrotron-based powder diffraction (SPD) to investigate difference envelope densities (DED). This method provides underexplored insights into residual electron densities between the activated pristine MOF and the activated composites, allowing for the elucidation of adsorption sites of guest species.[46] Within this particular composite system, DED was employed to obtain structural characteristics of the position of (1) infiltrated Pt-precursor molecules and (2) reduced elemental Pt-NPs in respect to their adsorption sites in the micropores and mesopores

of CYCU-3. Respective SPD patterns of pristine CYCU-3 and the composites Pt-precursor@MOF and **Pt-IWI-3** are shown in **Figure 8a**. The SPD patterns of both composites do not exhibit any shift in their reflections as compared to pristine CYCU-3, and most importantly, no new Bragg reflections of different phases are observed as evidenced from high-quality final Le Bail refinements. Final Le Bail refinement parameters are listed in **Table S2**. This SPD data enabled the generation of structure envelopes with respective DEDs of Pt-precursor@MOF and **Pt-IWI-3** shown in **Figure 8b**.[36] It is found that electron density of the Pt-precursor primarily concentrates around the Al-based metal nodes of CYCU-3 while populating both the micropores and mesopores. This adsorption site is no surprise since electrostatic interactions exist between the negatively charged Pt-precursor and the positively charged metal nodes. Upon reduction, the DED clearly shows significant electron density in the center of both pores, which is attributed to the high electron density of Pt-NPs, while no electron density remains around the metal nodes. The central nature of this adsorption site suggests that any distinct interactions with the pore walls can be excluded and that only single Pt-NPs are preset in the transverse direction of the pores. These results are also in good agreement with the Pt-NP formation process reported by Goia *et al*.[63] Similar to Pt-NP formation in solution, nucleation initiates within the pores followed by nuclei growth based on the diffusion of metal atoms through the channels of CYCU-3 ultimately forming the final Pt-NPs in which their aggregation is controlled by the pore environment, as confirmed by DED and TEM characterizations.

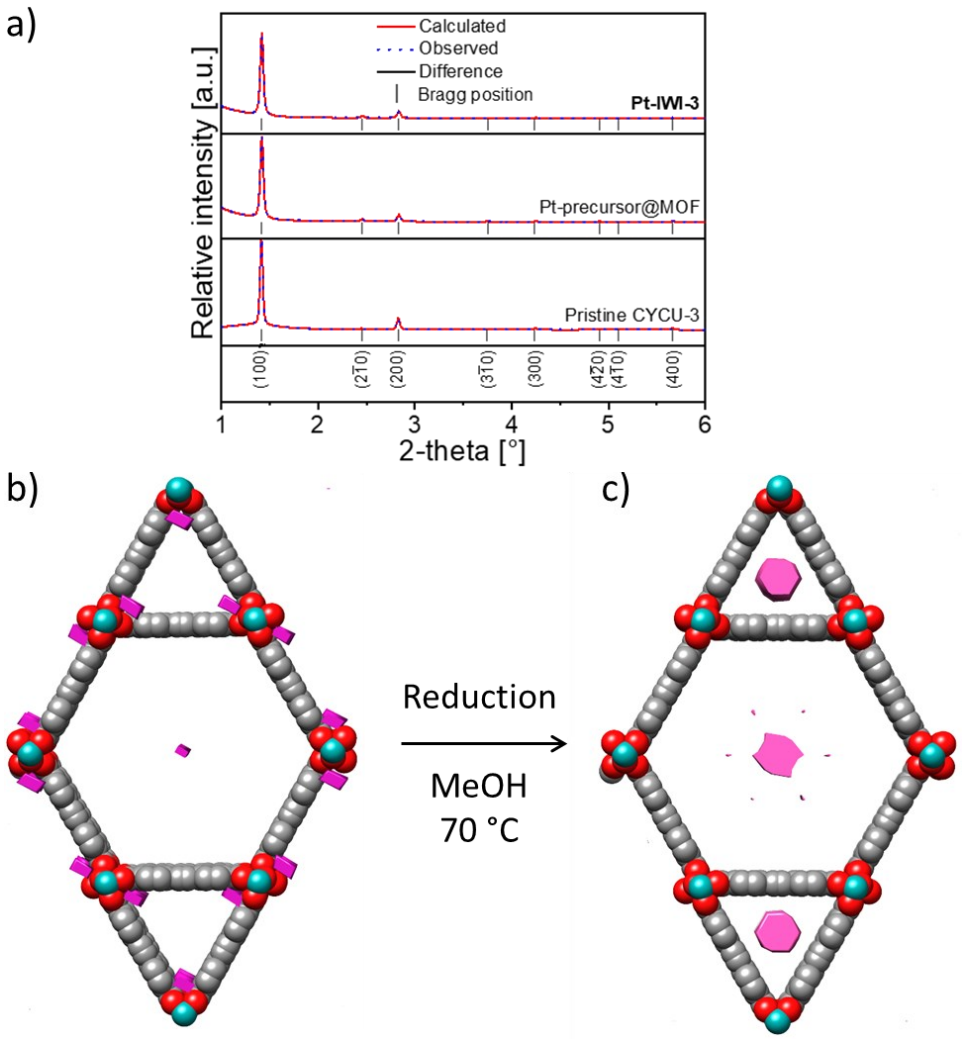

Figure 8. Final Le Bail whole pattern decomposition plots of the pristine MOF CYCU-3 compared with the composites Pt-precursor@MOF and **Pt-IWI-3** (a), and observed structure DEDs of Pt-precursor@MOF (b) and **Pt-IWI-3** (c) overlapped with a structural model of CYCU-3. The DEDs are defined as $\rho_{\Delta} = \rho_{\text{composite}} - \rho_{\text{MOF}}$ and shown in magenta.

Conclusions

This systematic study on the rational design and characterization of novel metal NP@MOF composites expands the understanding of potential materials for hydrogen storage applications. These materials can be fine-tuned for their physiochemical properties making them applicable within various temperature and pres-

sure ranges. We systematically synthesized and probed Pd- and Pt-based NP@MOF composites and furthered the understanding of different infiltration techniques including the well-established CVI method and a novel and "green" IWI method. A combination of modern solid-state analytical tools such as TEM and SPD-based DED were used to provide valuable mechanistic insight into the infiltration and reduction processes underlying the NP@MOF formation. Also, acknowledging that pure MOF materials such as record holders $Ni_2(DOBDC)$[16] with H_4DOBDC = 4,6-dioxido-1,3-benzenedicarboxylic acid, and $Be_{12}(OH)_{12}(BTB)_4$[17] with H_3BTB = 1,3,5-benzenetribenzoic acid, well exceed the performance of the herein presented composites, we want to highlight the opportunities which could evolve from the herein presented CVI and IWI processes for the development of new materials for applications beyond gas storage such as catalysis, a field strongly benefiting from the controlled formation of metal NPs embedded in porous matrices.

Acknowledgements

M.W. gratefully acknowledges Clarkson University for generous start-up funding and the National Science Foundation CAREER Program (Award No. 1752771) for support of this research. Work performed at the Advanced Photon Source at Argonne National Laboratory was supported by the U.S. Department of Energy, Office of Science, Office of Basic Energy Sciences, under Contract No. DE-AC02-06CH11357. We thank Christopher Plunkett from Clarkson University with assisting the TEM experiments. J.W. gratefully acknowledges funding by FuNaHybrid in the framework of the structural and excellence budget of Schleswig-Holstein strengthening the research at Universities of Applied Sciences.

Supporting Information

PXRD of as-synthesized CYCU-3, schematic representation of different experimental CVI setups, details on the CVI process conditions, Le Bail refinement parameters and plots, detailed DED parameters and

plots, low- and high pressure hydrogen isotherms of CVI samples, low- and high pressure hydrogen isotherms of as0synthezised CYCU-3, PXRD and nitrogen isotherms of IWI samples, DFT pore size distribution plots of CVI samples, SEM-EDS data of CVI and IWI samples, NP precursor loading time plots as function of various parameters, elemental mapping of IWI samples.

References

1. Suh, M. P.; Park, H. J.; Prasad, T. K.; Lim, D.-W. Hydrogen Storage in Metal–Organic Frameworks. *Chem. Rev. (Washington, DC, U. S.)* 2012, 112 (2), 782-835 DOI: 10.1021/cr200274s.
2. Rosen, M. A.; Koohi-Fayegh, S. The prospects for hydrogen as an energy carrier: an overview of hydrogen energy and hydrogen energy systems. *Energy, Ecology and Environment* 2016, 1 (1), 10-29 DOI: 10.1007/s40974-016-0005-z.
3. Zhao, D.; Yuan, D.; Zhou, H.-C. The current status of hydrogen storage in metal–organic frameworks. *Energy & Environmental Science* 2008, 1 (2), 222-235 DOI: 10.1039/B808322N.
4. Konda, S. K.; Chen, A. Palladium based nanomaterials for enhanced hydrogen spillover and storage. *Materials Today* 2016, 19 (2), 100-108 DOI: https://doi.org/10.1016/j.mattod.2015.08.002.
5. U.S. Department of Energy, Technical Targets for Onboard Hydrogen Storage for Light-Duty Vehicles, https://www.energy.gov/eere/fuelcells/doe-technical-targets-onboard-hydrogen-storage-light-duty-vehicles.
6. de la Casa-Lillo, M. A.; Lamari-Darkrim, F.; Cazorla-Amorós, D.; Linares-Solano, A. Hydrogen Storage in Activated Carbons and Activated Carbon Fibers. *The Journal of Physical Chemistry B* 2002, 106 (42), 10930-10934 DOI: 10.1021/jp014543m.
7. Jordá-Beneyto, M.; Suárez-García, F.; Lozano-Castelló, D.; Cazorla-Amorós, D.; Linares-Solano, A. Hydrogen storage on chemically activated carbons and carbon nanomaterials at high pressures. *Carbon* 2007, 45 (2), 293-303 DOI: https://doi.org/10.1016/j.carbon.2006.09.022.

8. Sevilla, M.; Alam, N.; Mokaya, R. Enhancement of Hydrogen Storage Capacity of Zeolite-Templated Carbons by Chemical Activation. *The Journal of Physical Chemistry C* 2010, 114 (25), 11314-11319 DOI: 10.1021/jp102464e.
9. Li, Y.; Yang, R. T. Hydrogen Storage in Low Silica Type X Zeolites. *The Journal of Physical Chemistry B* 2006, 110 (34), 17175-17181 DOI: 10.1021/jp0634508.
10. Kato, R.; Nishide, H. Polymers for carrying and storing hydrogen. *Polymer Journal* 2017, 50, 77 DOI: 10.1038/pj.2017.70.
11. Germain, J.; Fréchet, J. M. J.; Svec, F. Nanoporous Polymers for Hydrogen Storage. *Small* 2009, 5 (10), 1098-1111 DOI: 10.1002/smll.200801762.
12. Züttel, A.; Sudan, P.; Mauron, P.; Kiyobayashi, T.; Emmenegger, C.; Schlapbach, L. Hydrogen storage in carbon nanostructures. *International Journal of Hydrogen Energy* 2002, 27 (2), 203-212 DOI: https://doi.org/10.1016/S0360-3199(01)00108-2.
13. Atkinson, K.; Roth, S.; Hirscher, M.; Grünwald, W. Carbon nanostructures: An efficient hydrogen storage medium for fuel cells. *Fuel Cells Bulletin* 2001, 4 (38), 9-12 DOI: https://doi.org/10.1016/S1464-2859(01)80733-1.
14. Ahmed, A.; Seth, S.; Purewal, J.; Wong-Foy, A. G.; Veenstra, M.; Matzger, A. J.; Siegel, D. J. Exceptional hydrogen storage achieved by screening nearly half a million metal-organic frameworks. *Nature Communications* 2019, 10 (1), 1568 DOI: 10.1038/s41467-019-09365-w.
15. Balderas-Xicohténcatl, R.; Schlichtenmayer, M.; Hirscher, M. Volumetric Hydrogen Storage Capacity in Metal–Organic Frameworks. *Energy Technology* 2018, 6 (3), 578-582 DOI: 10.1002/ente.201700636.
16. Kapelewski, M. T.; Runčevski, T.; Tarver, J. D.; Jiang, H. Z. H.; Hurst, K. E.; Parilla, P. A.; Ayala, A.; Gennett, T.; FitzGerald, S. A.; Brown, C. M.; Long, J. R. Record High Hydrogen Storage Capacity in the Metal–Organic Framework Ni2(m-dobdc) at Near-Ambient Temperatures. *Chem. Mater.* 2018, 30 (22), 8179-8189 DOI: 10.1021/acs.chemmater.8b03276.

17. Sumida, K.; Hill, M. R.; Horike, S.; Dailly, A.; Long, J. R. Synthesis and Hydrogen Storage Properties of Be12(OH)12(1,3,5-benzenetribenzoate)4. *J. Am. Chem. Soc.* 2009, 131 (42), 15120-15121 DOI: 10.1021/ja9072707.
18. Meilikhov, M.; Yusenko, K.; Esken, D.; Turner, S.; Van Tendeloo, G.; Fischer, R. A. Metals@MOFs – Loading MOFs with Metal Nanoparticles for Hybrid Functions. *European Journal of Inorganic Chemistry* 2010, 2010 (24), 3701-3714 DOI: 10.1002/ejic.201000473.
19. Aulakh, D.; Islamoglu, T.; Bagundes, V. F.; Varghese, J. R.; Duell, K.; Joy, M.; Teat, S. J.; Farha, O. K.; Wriedt, M. Rational Design of Pore Size and Functionality in a Series of Isoreticular Zwitterionic Metal–Organic Frameworks. *Chemistry of Materials* 2018, 30 (22), 8332-8342 DOI: 10.1021/acs.chemmater.8b03885.
20. An, W.; Aulakh, D.; Zhang, X.; Verdegaal, W.; Dunbar, K. R.; Wriedt, M. Switching of Adsorption Properties in a Zwitterionic Metal–Organic Framework Triggered by Photogenerated Radical Triplets. *Chemistry of Materials* 2016, 28 (21), 7825-7832 DOI: 10.1021/acs.chemmater.6b03224.
21. Aulakh, D.; Varghese, J. R.; Wriedt, M. A New Design Strategy to Access Zwitterionic Metal–Organic Frameworks from Anionic Viologen Derivates. *Inorganic Chemistry* 2015, 54 (4), 1756-1764 DOI: 10.1021/ic5026813.
22. Rosi, N. L.; Eckert, J.; Eddaoudi, M.; Vodak, D. T.; Kim, J.; O'Keeffe, M.; Yaghi, O. M. Hydrogen Storage in Microporous Metal-Organic Frameworks. *Science* 2003, 300 (5622), 1127-1129 DOI: 10.1126/science.1083440.
23. Hu, Y. H.; Zhang, L. Hydrogen Storage in Metal–Organic Frameworks. *Advanced Materials* 2010, 22 (20), E117-E130 DOI: 10.1002/adma.200902096.
24. Langmi, H. W.; Ren, J.; North, B.; Mathe, M.; Bessarabov, D. Hydrogen Storage in Metal-Organic Frameworks: A Review. *Electrochimica Acta* 2014, 128, 368-392 DOI: https://doi.org/10.1016/j.electacta.2013.10.190.
25. Li, Y.; Yang, R. T. Gas Adsorption and Storage in Metal−Organic Framework MOF-177. *Langmuir* 2007, 23 (26), 12937-12944 DOI: 10.1021/la702466d.

26. Boufaden, N.; Pawelec, B.; Fierro, J. L. G.; Guil López, R.; Akkari, R.; Said Zina, M. Hydrogen storage in liquid hydrocarbons: Effect of platinum addition to partially reduced Mo-SiO2 catalysts. *Materials Chemistry and Physics* 2018, 209, 188-199 DOI: https://doi.org/10.1016/j.matchemphys.2018.01.061.
27. Li, Y.; Yang, R. T. Hydrogen Storage on Platinum Nanoparticles Doped on Superactivated Carbon. *The Journal of Physical Chemistry C* 2007, 111 (29), 11086-11094 DOI: 10.1021/jp072867q.
28. Adams, B. D.; Chen, A. The role of palladium in a hydrogen economy. *Materials Today* 2011, 14 (6), 282-289 DOI: https://doi.org/10.1016/S1369-7021(11)70143-2.
29. Valencia, F. J.; González, R. I.; Tramontina, D.; Rogan, J.; Valdivia, J. A.; Kiwi, M.; Bringa, E. M. Hydrogen Storage in Palladium Hollow Nanoparticles. *The Journal of Physical Chemistry C* 2016, 120 (41), 23836-23841 DOI: 10.1021/acs.jpcc.6b07895.
30. Yamauchi, M.; Kobayashi, H.; Kitagawa, H. Hydrogen Storage Mediated by Pd and Pt Nanoparticles. *ChemPhysChem* 2009, 10 (15), 2566-2576 DOI: 10.1002/cphc.200900289.
31. Li, Y.; Yang, R. T. Hydrogen Storage in Metal−Organic Frameworks by Bridged Hydrogen Spillover. *Journal of the American Chemical Society* 2006, 128 (25), 8136-8137 DOI: 10.1021/ja061681m.
32. Li, Y.; Yang, R. T. Significantly Enhanced Hydrogen Storage in Metal−Organic Frameworks via Spillover. *Journal of the American Chemical Society* 2006, 128 (3), 726-727 DOI: 10.1021/ja056831s.
33. Chen, L.; Chen, X.; Liu, H.; Li, Y. Encapsulation of Mono- or Bimetal Nanoparticles Inside Metal–Organic Frameworks via In situ Incorporation of Metal Precursors. *Small* 2015, 11 (22), 2642-2648 DOI: 10.1002/smll.201403599.
34. Rösler, C.; Fischer, R. A. Metal–organic frameworks as hosts for nanoparticles. *CrystEngComm* 2015, 17 (2), 199-217 DOI: 10.1039/C4CE01251H.

35. Lo, S.-H.; Chien, C.-H.; Lai, Y.-L.; Yang, C.-C.; Lee, J. J.; Raja, D. S.; Lin, C.-H. A mesoporous aluminium metal–organic framework with 3 nm open pores. *Journal of Materials Chemistry A* 2013, 1 (2), 324-329 DOI: 10.1039/C2TA00030J.
36. Aulakh, D.; Pyser, J. B.; Zhang, X.; Yakovenko, A. A.; Dunbar, K. R.; Wriedt, M. Metal–Organic Frameworks as Platforms for the Controlled Nanostructuring of Single-Molecule Magnets. *J. Am. Chem. Soc.* 2015, 137 (29), 9254-9257 DOI: 10.1021/jacs.5b06002.
37. Aulakh, D.; Xie, H.; Shen, Z.; Harley, A.; Zhang, X.; Yakovenko, A. A.; Dunbar, K. R.; Wriedt, M. Systematic Investigation of Controlled Nanostructuring of Mn12 Single-Molecule Magnets Templated by Metal–Organic Frameworks. *Inorganic Chemistry* 2017, 56 (12), 6965-6972 DOI: 10.1021/acs.inorgchem.7b00514.
38. Aulakh, D.; Liu, L.; Varghese, J. R.; Xie, H.; Islamoglu, T.; Duell, K.; Kung, C.-W.; Hsiung, C.-E.; Zhang, Y.; Drout, R. J.; Farha, O. K.; Dunbar, K. R.; Han, Y.; Wriedt, M. Direct Imaging of Isolated Single-Molecule Magnets in Metal–Organic Frameworks. *Journal of the American Chemical Society* 2019, 141 (7), 2997-3005 DOI: 10.1021/jacs.8b11374.
39. Proch, S.; Herrmannsdörfer, J.; Kempe, R.; Kern, C.; Jess, A.; Seyfarth, L.; Senker, J. Pt@MOF-177: Synthesis, Room-Temperature Hydrogen Storage and Oxidation Catalysis. *Chemistry – A European Journal* 2008, 14 (27), 8204-8212 DOI: 10.1002/chem.200801043.
40. Müller, M.; Lebedev, O. I.; Fischer, R. A. Gas-phase loading of [Zn4O(btb)2] (MOF-177) with organometallic CVD-precursors: inclusion compounds of the type [LnM]a@MOF-177 and the formation of Cu and Pd nanoparticles inside MOF-177. *Journal of Materials Chemistry* 2008, 18 (43), 5274-5281 DOI: 10.1039/B810989C.
41. Sabo, M.; Henschel, A.; Fröde, H.; Klemm, E.; Kaskel, S. Solution infiltration of palladium into MOF-5: synthesis, physisorption and catalytic properties. *Journal of Materials Chemistry* 2007, 17 (36), 3827-3832 DOI: 10.1039/B706432B.

42. Opelt, S.; Türk, S.; Dietzsch, E.; Henschel, A.; Kaskel, S.; Klemm, E. Preparation of palladium supported on MOF-5 and its use as hydrogenation catalyst. *Catalysis Communications* 2008, 9 (6), 1286-1290 DOI: https://doi.org/10.1016/j.catcom.2007.11.019.
43. Kim, H.; Chun, H.; Kim, G.-H.; Lee, H.-S.; Kim, K. Vapor phase inclusion of ferrocene and its derivative in a microporous metal–organic porous material and its structural characterization by single crystal X-ray diffraction. *Chemical Communications* 2006, (26), 2759-2761 DOI: 10.1039/B604925G.
44. Meilikhov, M.; Yusenko, K.; Fischer, R. A. The adsorbate structure of ferrocene inside [Al(OH)(bdc)]x (MIL-53): a powder X-ray diffraction study. *Dalton Transactions* 2009, (4), 600-602 DOI: 10.1039/B820882B.
45. Wriedt, M.; Sculley, J. P.; Yakovenko, A. A.; Ma, Y.; Halder, G. J.; Balbuena, P. B.; Zhou, H.-C. Low-Energy Selective Capture of Carbon Dioxide by a Pre-designed Elastic Single-Molecule Trap. *Angewandte Chemie International Edition* 2012, 51 (39), 9804-9808 DOI: 10.1002/anie.201202992.
46. Yakovenko, A. A.; Wei, Z.; Wriedt, M.; Li, J.-R.; Halder, G. J.; Zhou, H.-C. Study of Guest Molecules in Metal–Organic Frameworks by Powder X-ray Diffraction: Analysis of Difference Envelope Density. *Crystal Growth & Design* 2014, 14 (11), 5397-5407 DOI: 10.1021/cg500525g.
47. Petricek, V., Dusek, M., Palatinus L. . *Jana2006.Structure Determination Software Programs*. Institute of Physics: Praha, Czech Republic., 2006.
48. Zlotea, C.; Campesi, R.; Cuevas, F.; Leroy, E.; Dibandjo, P.; Volkringer, C.; Loiseau, T.; Férey, G.; Latroche, M. Pd Nanoparticles Embedded into a Metal-Organic Framework: Synthesis, Structural Characteristics, and Hydrogen Sorption Properties. *Journal of the American Chemical Society* 2010, 132 (9), 2991-2997 DOI: 10.1021/ja9084995.
49. Cheon, Y. E.; Suh, M. P. Enhanced Hydrogen Storage by Palladium Nanoparticles Fabricated in a Redox-Active Metal–Organic Framework. *Angewandte Chemie International Edition* 2009, 48 (16), 2899-2903 DOI: 10.1002/anie.200805494.

50. Kalidindi, S. B.; Oh, H.; Hirscher, M.; Esken, D.; Wiktor, C.; Turner, S.; Van Tendeloo, G.; Fischer, R. A. Metal@COFs: Covalent Organic Frameworks as Templates for Pd Nanoparticles and Hydrogen Storage Properties of Pd@COF-102 Hybrid Material. *Chemistry – A European Journal* 2012, 18 (35), 10848-10856 DOI: 10.1002/chem.201201340.
51. Zhou, H.; Zhang, J.; Zhang, J.; Yan, X.-F.; Shen, X.-P.; Yuan, A.-H. Spillover enhanced hydrogen storage in Pt-doped MOF/graphene oxide composite produced via an impregnation method. *Inorganic Chemistry Communications* 2015, 54, 54-56 DOI: https://doi.org/10.1016/j.inoche.2015.02.001.
52. Zhan, G.; Zeng, H. C. Hydrogen spillover through Matryoshka-type (ZIFs@)n−1ZIFs nanocubes. *Nature Communications* 2018, 9 (1), 3778 DOI: 10.1038/s41467-018-06269-z.
53. Prins, R. Hydrogen Spillover. Facts and Fiction. *Chemical Reviews* 2012, 112 (5), 2714-2738 DOI: 10.1021/cr200346z.
54. Sermon, P. A.; Bond, G. C. Hydrogen Spillover. *Catalysis Reviews* 1974, 8 (1), 211-239 DOI: 10.1080/01614947408071861.
55. Psofogiannakis, G. M.; Froudakis, G. E. Theoretical Explanation of Hydrogen Spillover in Metal−Organic Frameworks. *The Journal of Physical Chemistry C* 2011, 115 (10), 4047-4053 DOI: 10.1021/jp109541n.
56. Cheng, H.; Chen, L.; Cooper, A. C.; Sha, X.; Pez, G. P. Hydrogen spillover in the context of hydrogen storage using solid-state materials. *Energy & Environmental Science* 2008, 1 (3), 338-354 DOI: 10.1039/B807618A.
57. Hermes, S.; Schröter, M.-K.; Schmid, R.; Khodeir, L.; Muhler, M.; Tissler, A.; Fischer, R. W.; Fischer, R. A. Metal@MOF: Loading of Highly Porous Coordination Polymers Host Lattices by Metal Organic Chemical Vapor Deposition. *Angewandte Chemie International Edition* 2005, 44 (38), 6237-6241 DOI: 10.1002/anie.200462515.
58. Esken, D.; Turner, S.; Lebedev, O. I.; Van Tendeloo, G.; Fischer, R. A. Au@ZIFs: Stabilization and Encapsulation of Cavity-Size Matching Gold Clusters inside Functionalized Zeolite Imidazolate Frameworks, ZIFs. *Chemistry of Materials* 2010, 22 (23), 6393-6401 DOI: 10.1021/cm102529c.

59. Evans, J. D.; Sumby, C. J.; Doonan, C. J. Post-synthetic metalation of metal-organic frameworks. *Chem. Soc. Rev.* 2014, DOI: 10.1039/C4CS00076E.

60. Park, S.-J.; Lee, S.-Y. Hydrogen storage behaviors of platinum-supported multi-walled carbon nanotubes. *International Journal of Hydrogen Energy* 2010, 35 (23), 13048-13054 DOI: https://doi.org/10.1016/j.ijhydene.2010.04.083.

61. Mertens, F. O. Determination of absolute adsorption in highly ordered porous media. *Surface Science* 2009, 603 (10), 1979-1984 DOI: https://doi.org/10.1016/j.susc.2008.10.054.

62. Aijaz, A.; Akita, T.; Tsumori, N.; Xu, Q. Metal–Organic Framework-Immobilized Polyhedral Metal Nanocrystals: Reduction at Solid–Gas Interface, Metal Segregation, Core–Shell Structure, and High Catalytic Activity. *Journal of the American Chemical Society* 2013, 135 (44), 16356-16359 DOI: 10.1021/ja4093055.

63. V. Goia, D.; Matijević, E. Preparation of monodispersed metal particles. *New Journal of Chemistry* 1998, 22 (11), 1203-1215 DOI: 10.1039/A709236I.

64. Li, Y.; Yang, R. T. Hydrogen storage in metal-organic and covalent-organic frameworks by spillover. *AIChE Journal* 2008, 54 (1), 269-279 DOI: 10.1002/aic.11362.

65. Zhu, L.-G.; Xiao, H.-P. Gas Storages in Microporous Metal-Organic Framework at Ambient Temperature. *Zeitschrift für anorganische und allgemeine Chemie* 2008, 634 (5), 845-847 DOI: 10.1002/zaac.200700580.

66. Wang, L.; Stuckert, N. R.; Chen, H.; Yang, R. T. Effects of Pt Particle Size on Hydrogen Storage on Pt-Doped Metal−Organic Framework IRMOF-8. *The Journal of Physical Chemistry C* 2011, 115 (11), 4793-4799 DOI: 10.1021/jp111800c.

Table of Content Artwork

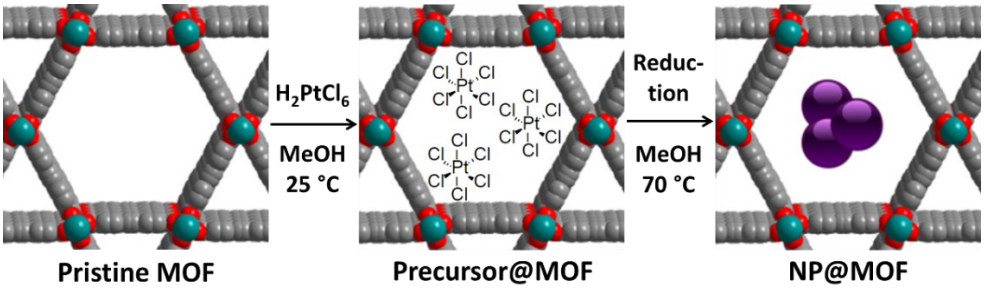

Synopsis

Chemical Vapor Infiltration (CVI) and Incipient Wetness Infiltration (IWI) processes were systematically explored to design novel Nanoparticle@Metal-Organic Framework (NP@MOF) composite materials for potential hydrogen storage applications. Room temperature hydrogen adsorption capacities of 0.95 and 0.20 mmol/g at 1 bar, and 2.9 and 1.8 mmol/g at 100 bar are found for CVI and IWI samples, respectively, and structural details regarding NP@MOF preparation were obtained through crystallographic means.